Article

Cell Reports

Myosin Va and Endoplasmic Reticulum Calcium Channel Complex Regulates Membrane Export during Axon Guidance

Graphical Abstract

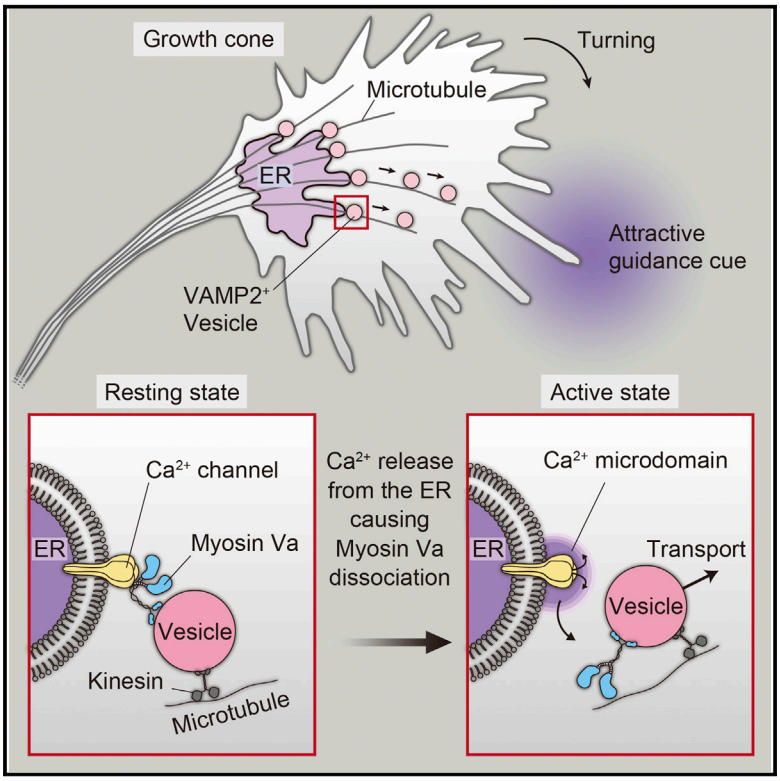

Highlights

- Myosin Va binds to ryanodine receptors and tethers membrane vesicles to the ER
- Myosin Va acts as a Ca^{2+} sensor near the ER to regulate targeted membrane export
- Photo-induced membrane export from the ER drives attractive growth cone turning
- The pathway dependent on myosin Va is likely to control axon guidance in vivo

Authors

Fumitaka Wada, Asuka Nakata, Yoshiro Tatsu, Noriko Ooashi, Tetsuko Fukuda, Takuji Nabetani, Hiroyuki Kamiguchi

Correspondence

kamiguchi@brain.riken.jp

In Brief

Wada et al. identify myosin Va as a Ca^{2+} sensor and effector near endoplasmic reticulum calcium channels and show that it mediates Ca^{2+}-induced membrane targeting to the cell surface for axon guidance, revealing an unexpected pathway for membrane trafficking.

Wada et al., 2016, Cell Reports *15*, 1329–1344
May 10, 2016
http://dx.doi.org/10.1016/j.celrep.2016.04.021

Cell Reports
Article

Myosin Va and Endoplasmic Reticulum Calcium Channel Complex Regulates Membrane Export during Axon Guidance

Fumitaka Wada,[1] Asuka Nakata,[1] Yoshiro Tatsu,[2] Noriko Ooashi,[1] Tetsuko Fukuda,[1] Takuji Nabetani,[1] and Hiroyuki Kamiguchi[1,*]
[1]RIKEN Brain Science Institute, 2-1 Hirosawa, Wako, Saitama 351-0198, Japan
[2]Health Research Institute, National Institute of Advanced Industrial Science and Technology (AIST), 2217-14 Hayashi-cho, Takamatsu, Kagawa 761-0395, Japan
*Correspondence: kamiguchi@brain.riken.jp
http://dx.doi.org/10.1016/j.celrep.2016.04.021

SUMMARY

During axon guidance, growth cones navigate toward attractive cues by inserting new membrane on the cue side. This process depends on Ca^{2+} release from endoplasmic reticulum (ER) Ca^{2+} channels, but the Ca^{2+} sensor and effector governing this asymmetric vesicle export remain unknown. We identified a protein complex that controls asymmetric ER Ca^{2+}-dependent membrane vesicle export. The Ca^{2+}-dependent motor protein myosin Va (MyoVa) tethers membrane vesicles to the ER via a common binding site on the two major ER Ca^{2+} channels, inositol 1,4,5-trisphosphate and ryanodine receptors. In response to attractive cues, micromolar Ca^{2+} from ER channels triggers MyoVa-channel dissociation and the movement of freed vesicles to the cue side, enabling growth cone turning. MyoVa-Ca^{2+} channel interactions are required for proper long-range axon growth in developing spinal cord in vivo. These findings reveal a peri-ER membrane export pathway for Ca^{2+}-dependent attraction in axon guidance.

INTRODUCTION

In neurons, membrane export is tightly regulated by Ca^{2+} to enable the precise spatial and temporal control of membrane vesicle biogenesis, storage, transport, and exocytosis at target membranes. The canonical Ca^{2+}-dependent synaptic vesicle release mechanism involves the fusion of docked synaptic vesicles with the neuronal plasma membrane after Ca^{2+} diffusion through voltage-gated Ca^{2+} channels (Parekh, 2008). In this system, specificity is achieved by the colocalization of a Ca^{2+} sensor synaptotagmin, the vesicle docking and priming machinery, and Ca^{2+} channels (Eggermann et al., 2011). However, for neurons that undergo long-distance axon migration guided by external cues, the synaptic vesicle release machinery is not well positioned to process membrane vesicles for fusion, nor does the presynaptic terminal allow control of the direction of vesicle targeting to the plasma membrane, because active zone release sites are non-mobile. Thus, a mobile Ca^{2+}-dependent vesicle export pathway for asymmetric axon guidance and constituent proteins that regulate asymmetric membrane export in growth cones remain unknown.

Insight into an uncharacterized Ca^{2+}-dependent vesicle export system for polarized cell migration might involve the growth cone endoplasmic reticulum (ER). The axon navigation machinery involves the translation of extracellular cues into directional migration toward their cellular targets (Huber et al., 2003; Tessier-Lavigne and Goodman, 1996). Such guidance cues attract or repel an axon by elevating cytosolic Ca^{2+} concentrations asymmetrically on the side of the growth cone facing higher concentrations of the cues (Gomez and Zheng, 2006; Henley and Poo, 2004; Henley et al., 2004; Tojima et al., 2011). Growth cone turning direction depends critically on the source of Ca^{2+}: Ca^{2+} release from the ER guides attraction whereas Ca^{2+} influx from the extracellular space induces repulsion if unaccompanied by Ca^{2+} release from the ER (Tojima et al., 2011). Downstream of these Ca^{2+} signals, asymmetric membrane trafficking mediates growth cone turning. Attractive Ca^{2+} signals from the ER facilitate centrifugal transport and exocytosis of vesicle-associated membrane protein 2 (VAMP2)-positive vesicles on the side of the growth cone with elevated Ca^{2+} (Akiyama and Kamiguchi, 2010; Tojima et al., 2007). However, the key molecule in growth cones that serves as a peri-ER sensor and effector for local Ca^{2+} signals that regulate asymmetric membrane vesicle export remains unknown.

Two types of ER-derived Ca^{2+} signals are known to mediate growth cone attraction (Akiyama et al., 2009; Ooashi et al., 2005): Ca^{2+}-induced Ca^{2+} release (CICR) through the ryanodine receptor type 3 (RyR3) and inositol 1,4,5-trisphosphate (IP_3)-induced Ca^{2+} release (IICR) through the IP_3 receptor (IP_3R). Both CICR and IICR promote centrifugal exocytic transport of VAMP2-positive vesicles for attractive growth cone turning, suggesting that the steering machinery can be triggered by elevations in cytosolic Ca^{2+} concentration from the ER. If RyR3 and IP_3R activate a common Ca^{2+} sensor that responds to Ca^{2+} microdomains arising from CICR and IICR on the ER, this could provide a long-sought explanation for how growth cones can discriminate between Ca^{2+} signaling for attractive and

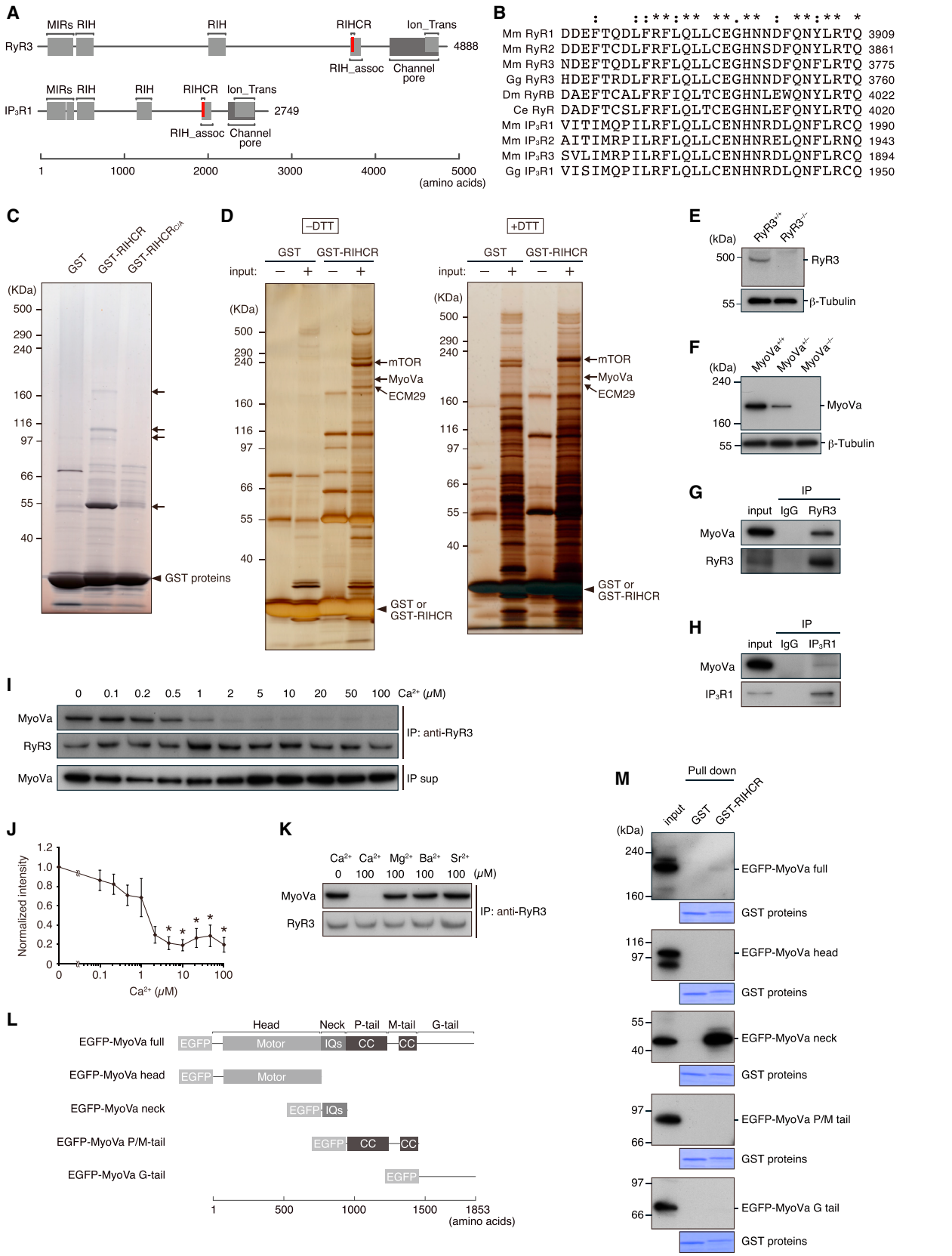

(legend on next page)

repulsive cues. Such a mechanism could be relevant to many cell types with membrane dynamics driven by ER Ca^{2+}. In this study, we sought to identify a Ca^{2+} sensor/effector that associates with the RyR3 and IP_3R and, in response to ER-derived Ca^{2+}, triggers asymmetric membrane export for growth cone attraction. We demonstrate a molecular mechanism for sensing ER Ca^{2+} and triggering directed membrane transport in response to external cues and show its in vivo significance for axon growth or guidance.

RESULTS

Ca^{2+}-Sensitive Binding of Myosin Va to ER Ca^{2+} Channels

We employed focal laser-induced photolysis (FLIP) of caged compounds to generate attractive or repulsive guidance signals in chick dorsal root ganglion (DRG) growth cones. Because the turning direction of growth cones after photolysis of caged Ca^{2+} depends on the occurrence of CICR, Ca^{2+}-elicited attraction can be converted to repulsion by pre-treating growth cones with a high dose of ryanodine that blocks RyR3 in DRG neurons (Ooashi et al., 2005). Also, photolysis of caged IP_3 induces growth cone attraction via generating IICR (Akiyama et al., 2009). We examined the effects of Ca^{2+} chelators on FLIP-induced growth cone turning and showed that BAPTA, but not EGTA, blocked attractive turning responses to CICR and IICR (Figure S1). By contrast, EGTA negated Ca^{2+}-elicited repulsion of growth cones (Figure S1F; ryanodine). This differential sensitivity to Ca^{2+} chelators suggested that CICR and IICR activate a Ca^{2+} sensor in close proximity to RyR3 and IP_3R, respectively. Both CICR and IICR induce growth cone attraction via centrifugal transport of membrane vesicles (Akiyama and Kamiguchi, 2010; Tojima et al., 2007); therefore, we examined the primary structures of RyR3 and IP_3R for a homologous sequence that could comprise a common binding site for a Ca^{2+} effector that drives attractive steering. These Ca^{2+} channels possess several homologous regions with low sequence identities (Ponting, 2000) as well as a highly homologous region (approximately 60% amino acid identities) consisting of 30 amino acids near the channel pore, which we termed the "RyR and IP_3R highly conserved region (RIHCR)" (Figure 1A). RIHCR is highly conserved across a wide range of species and subtypes of RyR and IP_3R (Figure 1B). Among the three RyR isoforms, only RyR3 is detectable in DRG neurons (Lokuta et al., 2002) and can mediate attractive guidance (Ooashi et al., 2005); therefore, in this study, we used the RIHCR sequence derived from RyR3.

To search for RIHCR-binding proteins, we conducted glutathione S-transferase (GST) pull-down assays using a GST-fused RIHCR peptide. Because GST-RIHCR can form multimers through a disulfide bond involving C3761 in RIHCR (Figure 1C), the assays were performed in the absence or presence of DTT (Figure 1D). Under both conditions, mass spectrometry identified three proteins that interacted with RIHCR, among which we selected myosin Va (MyoVa) as it participates in membrane transport (Hammer and Sellers, 2011). We generated specific antibodies against RyR3 and MyoVa (Figures 1E and 1F) and showed that, in mouse brain extracts, MyoVa co-immunoprecipitates with RyR3 (Figure 1G) and IP_3R type 1 (IP_3R1) (Figure 1H). We examined the Ca^{2+} dependence of binding and showed that Ca^{2+} concentrations over 2 μM reduced MyoVa co-immunoprecipitation with RyR3 (Figures 1I and 1J) whereas other divalent cations had no detectable effect even at 100 μM (Figure 1K). High Ca^{2+} did not reduce MyoVa in the supernatant (Figure 1I), excluding the possibility of MyoVa degradation by Ca^{2+}-dependent proteases. These data show that Ca^{2+} disrupts MyoVa

Figure 1. Identification of MyoVa as an RIHCR-Interacting Protein

(A) Schematic representation of RyR3 and IP_3R1 highlighting the channel pore and multiple homologous domains: protein mannosyltransferase, IP_3R and RyR regions (MIRs); RyR- and IP_3R-homology (RIH); RIH associated (RIH_assoc); ion transport (Ion_Trans); and RyR and IP_3R highly conserved region (RIHCR, highlighted in red).

(B) RIHCR amino acid sequences in RyR and IP_3R subtypes of *Mus musculus* (Mm), *Gallus gallus* (Gg), *Drosophila melanogaster* (Dm), and *Caenorhabditis elegans* (Ce). Identical conserved residues, conserved substitutions, and semi-conserved substitutions are marked with asterisks, semicolons, and dots, respectively. Numbers indicate the positions of rightmost amino acids.

(C) Silver staining of purified GST proteins separated by SDS-PAGE. The RIHCR sequence was derived from mouse RyR3. The arrowhead denotes monomers of GST proteins. The arrows denote higher-molecular-weight complexes that became undetectable or diminished when the cysteine residue 3761 in RIHCR was replaced by alanine ($GST\text{-}RIHCR_{C/A}$).

(D) Identification of RIHCR-interacting proteins. Glutathione beads coated with GST or GST-RIHCR (derived from mouse RyR3) were incubated with (+) or without (−) mouse brain lysates (input) in the absence (−DTT) or presence (+DTT) of the reducing agent DTT. Cellular proteins retained by the beads were separated by SDS-PAGE and visualized by silver staining. The arrows denote RIHCR-interacting proteins identified by mass spectrometry: mammalian target of rapamycin (mTOR); myosin Va (MyoVa); and proteasome-associated protein ECM29 homolog. The sequence coverage of MyoVa was 25% with 49 distinct peptides identified. The arrowhead denotes GST or GST-RIHCR retained by the beads.

(E) RyR3 immunoblots of $RyR3^{+/+}$ or $RyR3^{-/-}$ brain microsomal fractions. β-tubulin as a loading control is shown.

(F) MyoVa immunoblots of $MyoVa^{+/+}$, $MyoVa^{+/-}$, or $MyoVa^{-/-}$ spinal cord extracts.

(G and H) Immunoprecipitation (IP) with control IgG, anti-RyR3 (G), and anti-IP_3R1 (H) antibodies, followed by blotting with the indicated antibodies.

(I) RyR3 immunoprecipitation in the presence of increasing concentrations of Ca^{2+}. The immunoprecipitates and supernatants (IP sup) were blotted with the indicated antibodies.

(J) Quantification of MyoVa co-immunoprecipitation with RyR3. Immunoblot intensities of MyoVa normalized to those of RyR3 in RyR3 immunoprecipitates were plotted against Ca^{2+} concentrations (n = 4). The value in the absence of Ca^{2+} was arbitrarily presented as 1. *$p < 0.05$ versus zero Ca^{2+}.

(K) RyR3 immunoprecipitates prepared in the presence of divalent cations were blotted with the indicated antibodies.

(L) Schematic representation of EGFP-fused MyoVa and its fragments consisting of a motor domain (Motor), IQ motifs (IQs), or coiled-coil regions (CC).

(M) Identification of MyoVa binding site to RIHCR. Lysates of HEK293T cells expressing EGFP-fused proteins were incubated with GST or GST-RIHCR. Complexes recovered from glutathione beads were analyzed by EGFP immunoblotting and Coomassie brilliant blue (CBB) staining for detection of GST proteins. See also Figure S1.

binding to RyR3, suggesting that MyoVa is a candidate sensor for ER Ca^{2+} from RyR and IP_3R channels.

MyoVa is a homodimer with each monomer consisting of multiple domains: the N-terminal motor head interacting with filamentous actin (head); the neck containing six IQ motifs in tandem (neck); the proximal/medial tail containing coiled-coil regions for dimerization (P-tail and M-tail); and the C-terminal globular tail that binds cargos such as synaptic vesicles (G-tail; Figure 1L; Espreafico et al., 1992). To identify the region of MyoVa that binds to RyR3, we performed GST pull-down assays with lysates of HEK293T cells expressing EGFP-fused MyoVa fragments. These assays indicated that only the MyoVa neck region interacted with GST-RIHCR (Figures 1L and 1M). Because the myosin neck region is not known to associate with motor cargo or cytoskeleton, these data suggest that MyoVa can bind to the RyR3 via the neck region without direct interference of MyoVa's association with cargos or filamentous actin.

MyoVa Is Necessary for Ca^{2+}-Induced Growth Cone Guidance

The secondary structure of RIHCR was predicted to be mainly α helices, suggesting that its hydrophilic residues are exposed to the external space and can mediate MyoVa interaction with RIHCR. We therefore synthesized GST-fused RIHCR peptides with each conserved hydrophilic residue replaced by alanine (Figure S2A) and examined their binding to MyoVa. GST pull-down assays revealed that RIHCR interaction with MyoVa was marginally attenuated by E3762A or D3767A and abolished by E3762A and D3767A double mutations (ED/AA) (Figure S2B). Also, the ED/AA mutation negated RIHCR binding to MyoVa neck domain (Figure S2C). Consistent with our hypothesis that RIHCR in RyR3 mediates RyR3 interaction with MyoVa, exogenously applied RIHCR peptide, but not a scrambled sequence (RIHCRscr) or RIHCR with the ED/AA mutation ($RIHCR_{ED/AA}$), disrupted MyoVa co-immunoprecipitation with RyR3 (Figure 2A). We then injected these peptides into DRG neurons to test whether attractive growth cone turning requires the MyoVa interaction with ER Ca^{2+} channels. Growth cone attraction induced by FLIP of caged Ca^{2+} was converted to repulsion in neurons preloaded with RIHCR, but not RIHCRscr or $RIHCR_{ED/AA}$ (Figures 2B–2D). This conversion was not attributable to impaired Ca^{2+} release from the ER because RIHCR loading did not inhibit CICR that accompanied FLIP-induced Ca^{2+} elevations (Figure S3). These results suggest that, if MyoVa stays dissociated from ER Ca^{2+} channels, then CICR in attractive Ca^{2+} signals cannot activate the steering machinery for attraction whereas other Ca^{2+} components remain active in triggering repulsive turning. RIHCR loading also blocked growth cone attraction induced by FLIP of caged IP_3 (Figures S4A–S4C). The peptide loading had no detectable effect on axon growth: the length of RIHCR-loaded axons (105.1 ± 2.7 μm; n = 99) and $RIHCR_{ED/AA}$-loaded axons (108.5 ± 3.7 μm; n = 110) was indistinguishable from that of unloaded axons (102.2 ± 2.7 μm; n = 108).

We further examined the involvement of MyoVa in growth cone attraction using DRG neurons derived from mice with a spontaneous null mutation of MyoVa (also known as "dilute lethal"; Mercer et al., 1991). The loss of MyoVa expression converted attraction to repulsion in assays of growth cone turning induced by FLIP of caged Ca^{2+} (Figures 2E–2G) and of caged IP_3 (Figures S4D–S4F). There was no significant difference in axon growth between $MyoVa^{+/+}$ (111.7 ± 4.1 μm; n = 105) and $MyoVa^{-/-}$ neurons (107.2 ± 4.7 μm; n = 101). To test whether MyoVa also participates in physiological cue-mediated axon guidance, we assessed growth cone responses to an extracellular gradient of myelin-associated glycoprotein (MAG) (Henley et al., 2004) because MAG-induced attraction depends on CICR through RyR (Tojima et al., 2014). As expected, MAG gradients attracted $MyoVa^{+/+}$ axons but repelled $MyoVa^{-/-}$ axons (Figures 2H–2J). Collectively, our results indicate that MyoVa expression and its interaction with ER Ca^{2+} channels is a prerequisite for CICR and IICR to induce growth cone attraction.

MyoVa Is Necessary for Ca^{2+}-Induced Membrane Export

CICR or IICR on one side of the growth cone causes attractive turning via centrifugal transport of membrane vesicles, which carry VAMP2 and can be labeled with the fluorescent lipophilic probe FM1-43 (Akiyama and Kamiguchi, 2010; Tojima et al., 2007). We therefore tested whether MyoVa association with ER Ca^{2+} channels participates in CICR/IICR-induced transport of FM1-43-labeled (Figures 3A–3C and S7) and VAMP2-positive (Figures 3D and 3E) vesicles. To visualize intracellular VAMP2-positive vesicles, we transfected neurons with a construct containing improved ratiometric pHluorin (iR-pHluorin) fused to the luminal end of VAMP2 (VAMP2-iR-pHluorin) because iR-pHluorin is practically nonfluorescent at extracellular pH (~7.4) but can emit fluorescence below the intravesicular pH (~5.5; Katayama et al., 2011). To evaluate the spatial correlation between guidance signals and migrating vesicles, we generated CICR/IICR in a broader area, i.e., approximately half of the growth cone peripheral domain, and compared organelle dynamics between both sides of the growth cone. Such broader signals were generated by photolysis of caged Ca^{2+} or caged IP_3 using UV light from a xenon light source passed through a pinhole. Similarly to FLIP-induced Ca^{2+} elevations, these broader Ca^{2+} signals on one side of the growth cone induced attractive turning, which was converted to repulsion after loading of RIHCR, but not $RIHCR_{ED/AA}$, peptides (Figure S5). Consistent with our previous observations (Akiyama and Kamiguchi, 2010; Tojima et al., 2007), unilateral CICR or IICR in growth cones increased the number of vesicles migrating from the central (C)- to peripheral (P)-domain only on the side with the Ca^{2+} signals (Figures 3A, 3B, 3D, 3E, and S7A; control; Movie S1). The directional movement of these vesicles was confirmed by analyzing their trajectories in the growth cone P-domain (Figure S6). An estimation in our previous study (Tojima et al., 2007) showed that, within 10 min after the onset of CICR, asymmetric vesicle transport causes a 30% increase in the surface area of growth cone plasmalemma on the side with CICR, which is sufficient to generate asymmetric plasmalemmal expansion for growth cone turning. Intracellular loading of RIHCR peptide increased the basal level of centrifugal transport of FM1-43-labeled and VAMP2-positive vesicles and negated CICR-induced asymmetry, whereas RIHCRscr or $RIHCR_{ED/AA}$ control peptides had no detectable effect (Figures 3B and 3E). Similarly, RIHCR, but not $RIHCR_{ED/AA}$, abolished the IICR-induced

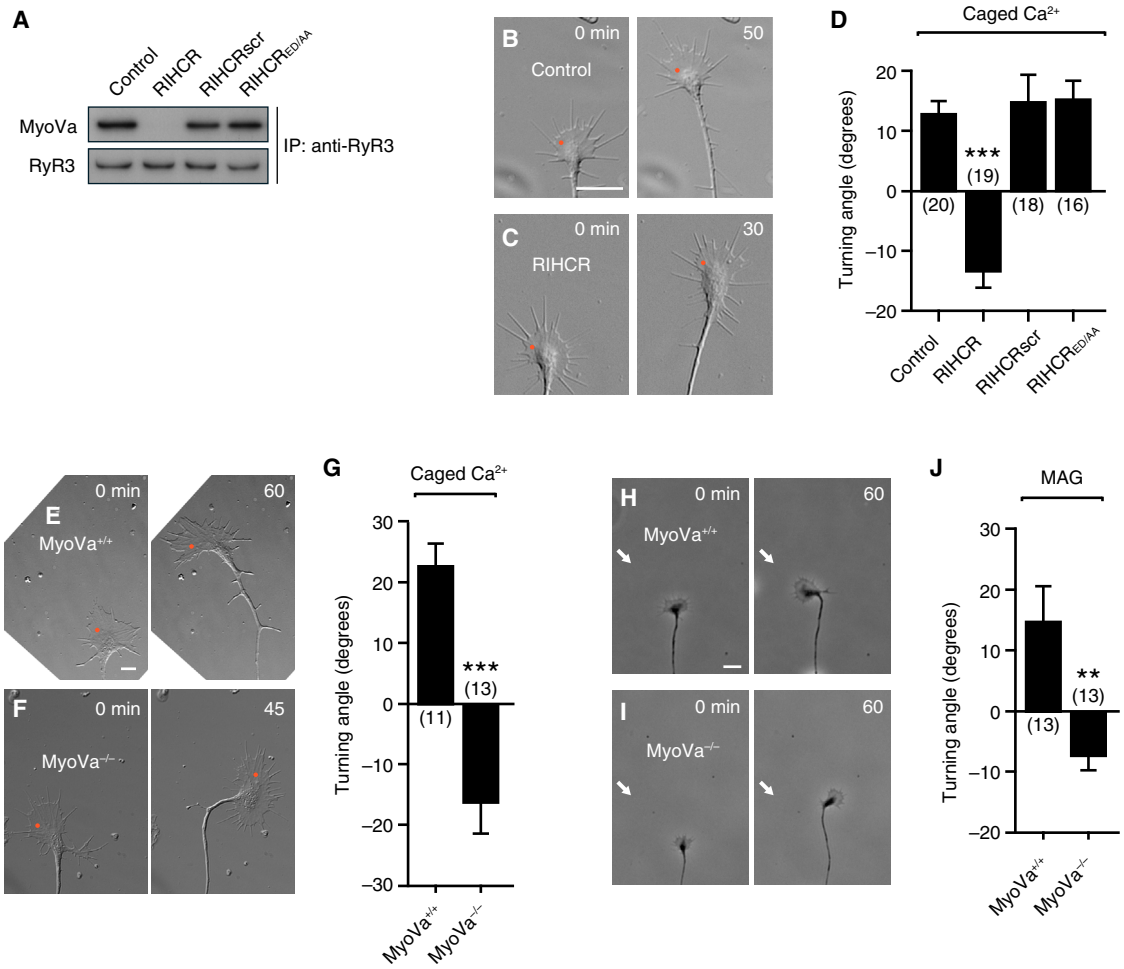

Figure 2. Growth Cone Attraction Involves MyoVa Interaction with ER Ca^{2+} Channels

(A) RyR3 immunoprecipitation in the absence (control) or presence of RIHCR peptides followed by immunoblotting.

(B and C) Time-lapse differential interference contrast (DIC) images of unloaded (B) or RIHCR-loaded (C) chick DRG growth cones. Attractive Ca^{2+} signals were generated by FLIP of caged Ca^{2+} at red spots. Time in minutes after the onset of repetitive FLIP (3 s interval) is shown. The scale bar represents 10 μm.

(D) Turning responses of unloaded (control) or peptide-loaded growth cones to FLIP of caged Ca^{2+}. Positive and negative values represent attractive and repulsive turning angles, respectively. Numbers in parentheses indicate the total number of growth cones examined. ***$p < 0.001$ versus control.

(E and F) Time-lapse images of MyoVa$^{+/+}$ (E) and MyoVa$^{-/-}$ (F) mouse growth cones, showing their turning responses to FLIP of caged Ca^{2+} at red spots. The scale bar represents 10 μm.

(G) Turning angles of MyoVa$^{+/+}$ and MyoVa$^{-/-}$ growth cones in response to FLIP of caged Ca^{2+}. ***$p < 0.001$.

(H and I) Time-lapse phase-contrast images of MyoVa$^{+/+}$ (H) and MyoVa$^{-/-}$ (I) growth cones exposed to MAG gradients (arrows). Time in minutes after the onset of MAG application is shown. The scale bar represents 10 μm.

(J) Turning angles of MyoVa$^{+/+}$ and MyoVa$^{-/-}$ growth cones in MAG gradients. **$p < 0.01$.

See also Figures S2–S4.

asymmetric transport of FM1-43-labeled vesicles (Figure S7A). The increased basal level of vesicle transport after RIHCR loading implicates MyoVa association with ER Ca^{2+} channels in the suppression of vesicle transport and suggests that MyoVa may dissociate from ER Ca^{2+} channels in response to Ca^{2+} elevations (Figures 1I–1K) to initiate centrifugal vesicle export. We analyzed MyoVa$^{-/-}$ growth cones and showed a requirement of MyoVa for CICR/IICR-induced asymmetry in vesicle transport (Figures 3C and S7B). These data indicate that the MyoVa interaction with ER Ca^{2+} channels is a prerequisite for peri-ER membrane export driven by CICR and IICR.

The globular tail domain of MyoVa is essential for cargo recognition (Reck-Peterson et al., 2000) and interacts with various adaptor proteins including VAMP2 on vesicles (Fukuda et al., 2002; Ohyama et al., 2001). This finding, together with MyoVa-RyR3 binding (Figure 1), raised the possibility that MyoVa tethers VAMP2-positive vesicles to RyR3 on the ER. Because it was difficult to evaluate colocalization of VAMP2 and RyR3 in conventional immunofluorescence (Figure 4A), their colocalization was examined using proximity ligation assays (PLA) in which oligonucleotides attached to antibodies against the two proteins can be ligated and labeled with fluorescent probes when located

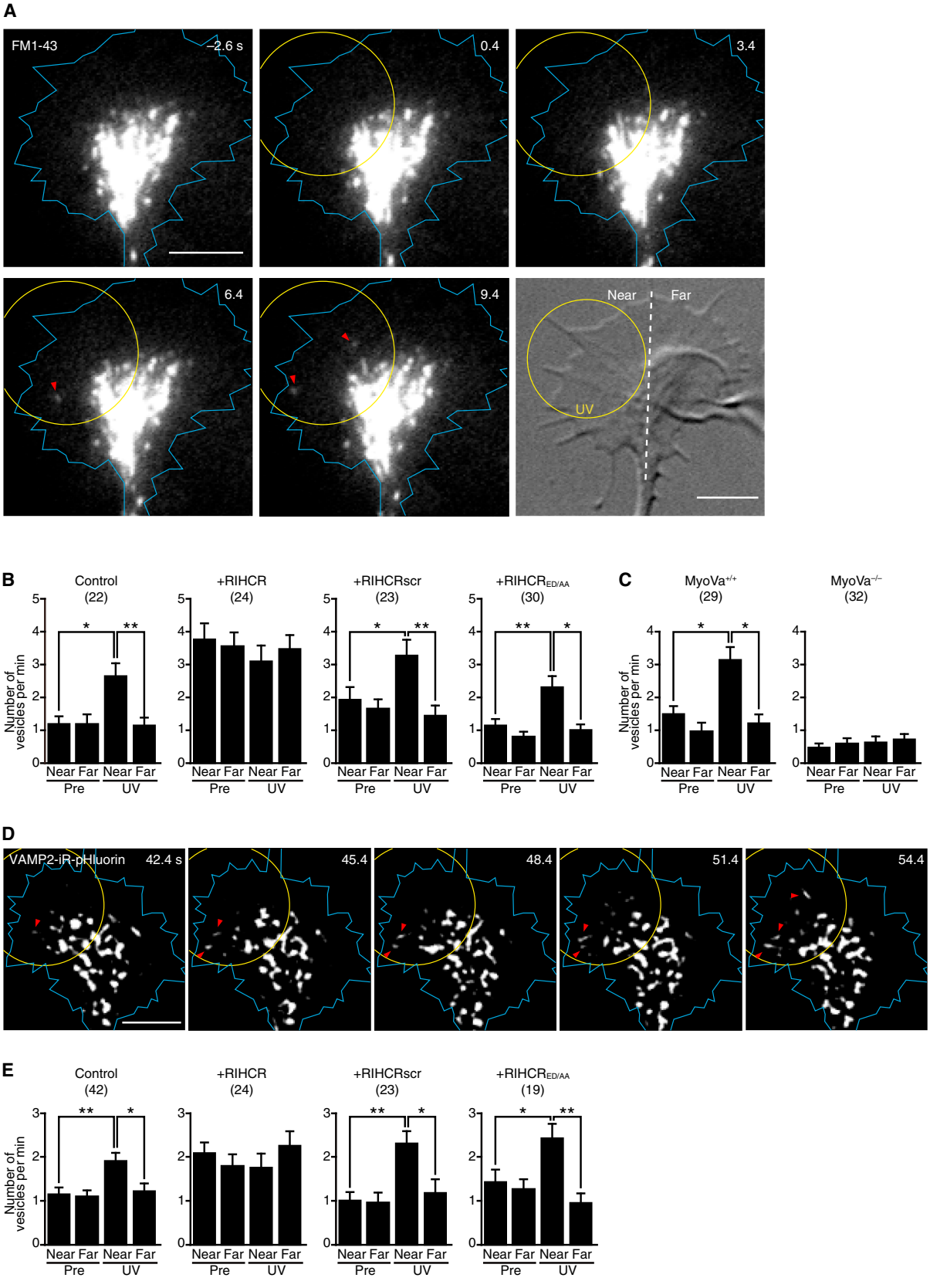

(legend on next page)

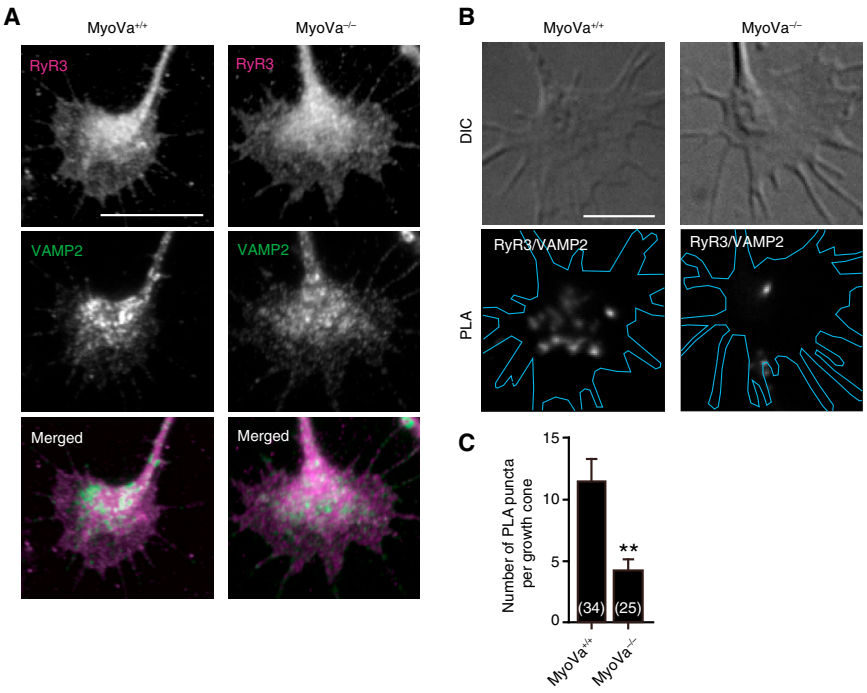

Figure 4. MyoVa Mediates VAMP2 Colocalization with RyR3

(A) Double immunofluorescence of RyR3 (magenta) and VAMP2 (green) in MyoVa$^{+/+}$ or MyoVa$^{-/-}$ growth cone. The scale bar represents 10 μm.

(B) Detection of the close positioning of VAMP2 and RyR3 by PLA. Shown are PLA signals and corresponding DIC images of MyoVa$^{+/+}$ or MyoVa$^{-/-}$ growth cone. The margins of the growth cone are outlined in blue. The scale bar represents 5 μm.

(C) Quantification of PLA signals as assessed by the number of PLA puncta per growth cone. Numbers in parentheses indicate the total number of growth cones examined. **$p < 0.01$.

within 40 nm of each other (Söderberg et al., 2006). MyoVa$^{+/+}$ growth cones exhibited PLA signals representing the colocalization of VAMP2 and RyR3 (Figures 4B and 4C). However, the loss of MyoVa expression decreased PLA signals (Figures 4B and 4C), consistent with the MyoVa-mediated tethering of VAMP2 vesicles to ER Ca^{2+} channels.

MyoVa-ER Ca^{2+} Channel Dissociation Triggers Vesicle Transport

If CICR facilitates centrifugal vesicle export via disrupting MyoVa-mediated tethering of VAMP2 vesicles to RyR3, then an experimental dissociation of MyoVa from the RyR3 should be sufficient to initiate vesicle transport. We designed and synthesized a caged RIHCR peptide (cgRIHCR), in which the two essential amino acids E3762 and D3767 for RIHCR binding to MyoVa were masked by the caging group 1-(4,5-dimethoxy-2-nitrophenyl)ethanol (Figure 5A). Whereas non-photolyzed cgRIHCR did not perturb MyoVa co-immunoprecipitation with RyR3, photolyzed cgRIHCR reduced MyoVa co-immunoprecipitation with RyR3 (Figure 5B), indicating that cgRIHCR causes MyoVa dissociation from RyR3 only after photolysis. We also synthesized a scrambled caged peptide (cgRIHCRscr) that had no detectable effect on MyoVa interaction with RyR3 even after photolysis (Figures 5A and 5B). Mass spectrometric analyses of cgRIHCR and cgRIHCRscr confirmed UV-induced release of their caging groups and the production of intact peptides.

Photolysis of intracellularly injected cgRIHCR, but not cgRIHCRscr, on one side of the growth cone facilitated centrifugal migration of FM1-43-labeled vesicles only on the side with UV irradiation (Figures 5C and 5D; Movie S2). As another control, loading of pre-uncaged cgRIHCR increased the basal level of vesicle transport but did not further facilitate vesicle transport upon UV irradiation (Figure 5D). The microtubule-depolymerizing reagent nocodazole abolished asymmetric vesicle transport induced by cgRIHCR photolysis (Figure 5D), indicating that the observed vesicle transport after the production of RIHCR peptides is dependent on intact microtubules. cgRIHCR photolysis elicited vesicle transport even in the presence of intracellular BAPTA (Figure 5D), consistent with our model that MyoVa dissociation from ER Ca^{2+} channels acts downstream of Ca^{2+} signals. We also found that cgRIHCR photolysis facilitated vesicle transport in MyoVa$^{+/+}$, but not MyoVa$^{-/-}$, growth cones, indicating that MyoVa is required for this membrane trafficking event (Figure 5E). Using neurons expressing VAMP2-iR-pHluorin, we showed that the photolysis of cgRIHCR, but not cgRIHCRscr,

Figure 3. CICR-Induced Membrane Transport Involves MyoVa Interaction with ER Ca^{2+} Channels

(A) Time-lapse fluorescence and DIC images of a growth cone loaded with FM1-43. After the onset of attractive Ca^{2+} signals generated by caged Ca^{2+} photolysis, endocytic vesicles labeled with FM1-43 (red arrowheads) showed centrifugal migration from the C- to P-domain on the side with the Ca^{2+} signals. Yellow circles denote the area exposed to UV pulses. Time in seconds after the onset of repetitive photolysis is shown. The margins of the growth cone are outlined in blue. The scale bars represent 5 μm.

(B and C) Frequencies of centrifugal migration of FM1-43-labeled vesicles before (pre) and after (UV) caged Ca^{2+} photolysis, on the photolysis (near) and opposite (far) sides of the growth cone. The effects of CICR were assessed in unloaded (control) and peptide-loaded growth cones (B) or in MyoVa$^{+/+}$ and MyoVa$^{-/-}$ growth cones (C). Numbers in parentheses indicate the total number of growth cones examined. *$p < 0.05$; **$p < 0.01$.

(D) Growth cone expressing VAMP2-iR-pHluorin, in which fluorescent vesicles (red arrowheads) showed centrifugal migration on the side with attractive Ca^{2+} signals (yellow circles). The scale bar represents 5 μm.

(E) Frequencies of centrifugal migration of VAMP2-iR-pHluorin vesicles before (pre) and after (UV) caged Ca^{2+} photolysis, on the near and far sides of the unloaded (control) and peptide-loaded growth cone. *$p < 0.05$; **$p < 0.01$.

See also Figures S5–S7 and Movie S1.

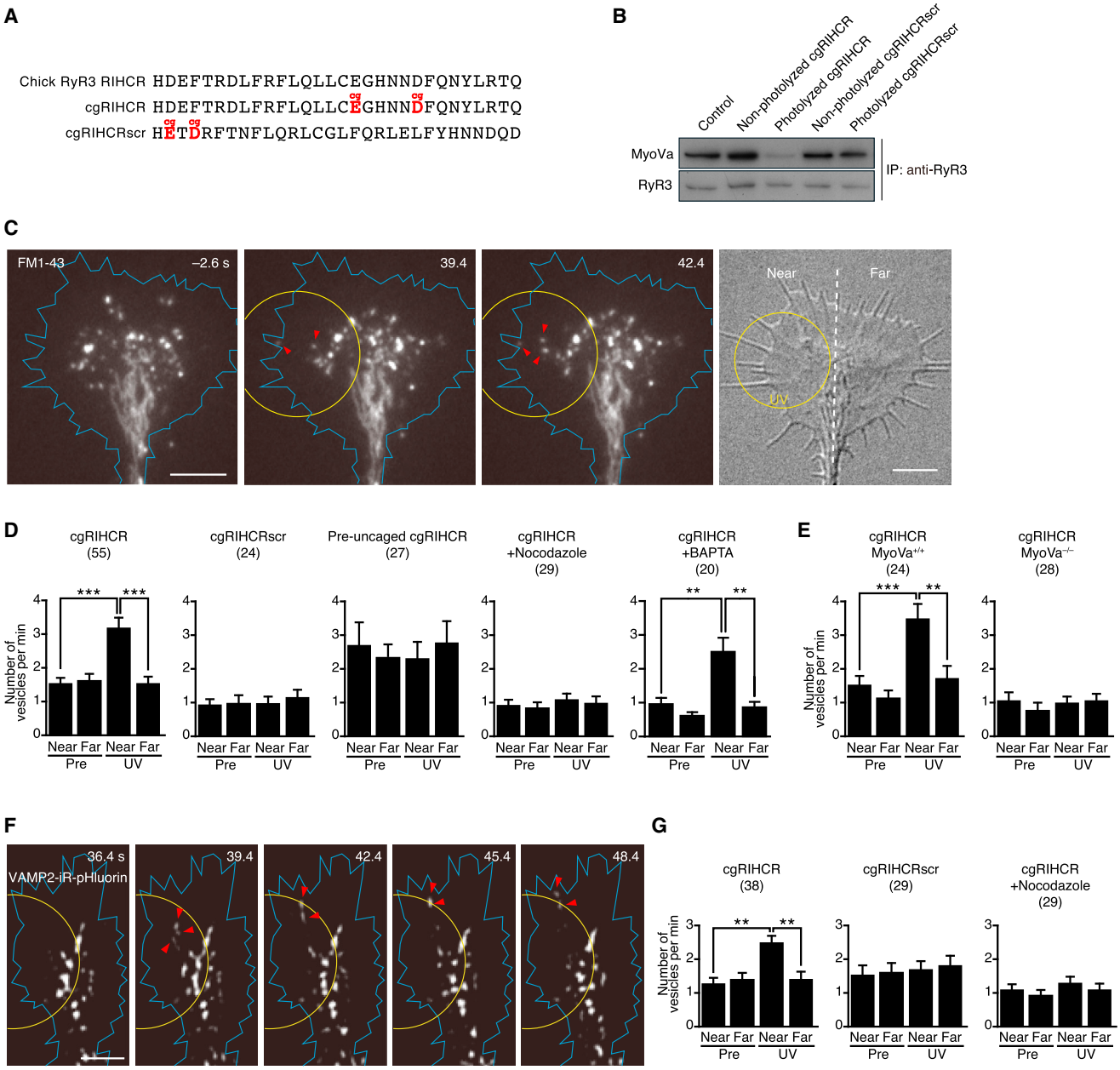

Figure 5. MyoVa Dissociation from ER Ca^{2+} Channels Elicits Vesicle Transport

(A) Amino acid sequences of caged RIHCR (cgRIHCR) and its scrambled version (cgRIHCRscr). The caged glutamate and aspartate are highlighted in red.

(B) RyR3 immunoprecipitates in the absence (control) or presence of the indicated peptides were blotted with anti-MyoVa and anti-RyR3 antibodies.

(C) Time-lapse fluorescence and DIC images of a growth cone loaded with FM1-43, showing centrifugal vesicle migration (red arrowheads) on the side with cgRIHCR photolysis (yellow circles). Time in seconds after the onset of repetitive photolysis is shown. The margins of the growth cone are outlined in blue. The scale bars represent 5 μm.

(D) Frequencies of centrifugal migration of FM1-43-labeled vesicles before (pre) and after (UV) the onset of repetitive UV irradiation, on the near and far sides of the growth cone loaded with the following peptides: cgRIHCR; cgRIHCRscr; or cgRIHCR that had been uncaged before loading (pre-uncaged). The effect of intracellular BAPTA and bath-applied nocodazole was also tested. Numbers in parentheses indicate the total number of growth cones examined. $^{**}p < 0.01$; $^{***}p < 0.001$.

(E) Frequencies of centrifugal migration of FM1-43-labeled vesicles before and after cgRIHCR photolysis in MyoVa$^{+/+}$ or MyoVa$^{-/-}$ growth cones. $^{**}p < 0.01$; $^{***}p < 0.001$.

(F) Time-lapse images of a growth cone showing centrifugal migration of VAMP2-iR-pHluorin vesicles (red arrowheads) on the side with cgRIHCR photolysis (yellow circles). The scale bar represents 5 μm.

(G) Frequencies of centrifugal migration of VAMP2-iR-pHluorin vesicles before and after photolysis of the indicated peptides. The effect of nocodazole was also tested. $^{**}p < 0.01$.

See also Movies S2 and S3.

elicited microtubule-dependent transport of VAMP2 vesicles (Figures 5F and 5G; Movie S3). These results suggest that MyoVa dissociation from ER Ca^{2+} channels is sufficient to initiate centrifugal transport of VAMP2 membrane vesicles.

MyoVa-ER Ca^{2+} Channel Dissociation Enables Attractive Axon Guidance

If MyoVa dissociation from ER Ca^{2+} channels mediates growth cone attraction via centrifugal transport of VAMP2 vesicles, these vesicles should be exocytosed at the growth cone P-domain, leading to the asymmetric recruitment of plasmalemmal components and associated molecules (Tojima et al., 2007). To monitor VAMP2-mediated exocytosis, we transfected neurons with a construct of pH-sensitive Venus fused to the luminal end of VAMP2 (pHVenus-VAMP2) because pHVenus is practically nonfluorescent below intravesicular pH (~5.5) and its emission greatly increases at extracellular pH (~7.4; Tojima et al., 2007). Photolysis of cgRIHCR, but not cgRIHCRscr, on one side of the growth cone caused an asymmetric increase of pHVenus fluorescence in the P-domain (Figures 6A–6C). This asymmetric signal was abolished by nocodazole (Figures 6B and 6C), suggesting that cgRIHCR photolysis enhances VAMP2-mediated exocytosis after microtubule-dependent vesicle transport into the P-domain. We also showed that single cgRIHCR photolysis by one-shot UV irradiation of 100-ms duration increased pHVenus-VAMP2 fluorescence only on the near side of growth cones with a decay half-life ($t_{1/2}$) of 10.6 ± 1.4 s (Figure 6D). This result suggests that, after peri-ER membrane export, exocytosed membranes remain within the growth cone plasmalemma for at least 10 s.

We next examined the effect of cgRIHCR photolysis on growth cone turning. Growth cones loaded with cgRIHCR, but not cgRIHCRscr or pre-uncaged cgRIHCR, turned toward the side with UV irradiation (Figures 6E and 6F). This turning was blocked by nocodazole or tetanus neurotoxin (TeNT) that cleaves VAMP2 (Figure 6F), suggesting the involvement of microtubule-dependent transport and VAMP2-mediated exocytosis of membrane vesicles. Remarkably, cgRIHCR photolysis elicited growth cone turning even in the presence of intracellular BAPTA (Figure 6F), indicating that peri-ER membrane export is sufficient to initiate attractive steering independent of Ca^{2+} signals. The involvement of MyoVa was further confirmed by loss of turning after cgRIHCR photolysis of MyoVa$^{-/-}$ growth cones (Figures 6G–6I). We conclude that MyoVa dissociation from ER Ca^{2+} channels downstream of attractive Ca^{2+} signals elicits centrifugal transport and VAMP2-mediated exocytosis of membrane vesicles for growth cone attractive guidance.

MyoVa-ER Ca^{2+} Channel Complex Mediates Spinal Cord Axon Guidance In Vivo

To demonstrate physiological significance of ER-driven membrane export, we investigated whether this molecular pathway also operates in axon guidance in vivo. In developing spinal cord, the floor plate (FP) at the ventral midline produces netrin-1 and sonic hedgehog to attract commissural axons (Dickson and Zou, 2010). It is also known that CICR mediates growth cone attractive responses to netrin-1 (Hong et al., 2000). We therefore transfected spinal cords of Hamburger-Hamilton stage 14 (HH14) chick embryos (Hamburger and Hamilton, 1951) with a plasmid encoding either RIHCR or RIHCR$_{ED/AA}$ sequence and analyzed the trajectory of commissural axons at HH23–24 (Figure 7A). The transfected cells were visualized with enhanced yellow fluorescent protein (EYFP) and the FP with the anti-HNF-3β antibody (Parra and Zou, 2010). Open-book preparations of control spinal cords (transfected with EYFP only) showed that the majority of commissural axons had crossed the FP (Figures 7B and 7E). In contrast, RIHCR-transfected axons failed to reach and cross the FP although RIHCR$_{ED/AA}$ had no detectable effect on commissural axon guidance (Figures 7C–7E). RIHCR or RIHCR$_{ED/AA}$ did not significantly alter the total number of EYFP-positive axons (Figure 7F). The involvement of MyoVa in commissural axon guidance was also confirmed using MyoVa$^{-/-}$ mice. We injected the lipophilic dye 1,1'-dioctadecyl-3,3,3′3'-tetramethylindocarbocyanine perchlorate (DiI) to the dorsal region of spinal cord open-book preparations at embryonic day 11.5 and analyzed the trajectory of commissural axons (Figure 7G). Although the majority of MyoVa$^{+/+}$ commissural axons had crossed the FP, MyoVa$^{-/-}$ axons failed to reach and cross the FP at the same developmental stage (Figures 7H–7J). Although we cannot rule out possible selective effects on axon growth in these studies, owing to the potential impact of membrane addition on overall growth cone position that cannot be separated from guidance per se, these results support a role for the MyoVa interaction with ER Ca^{2+} channels underlying attractive axon growth and guidance in development.

DISCUSSION

In this study, we report (1) an asymmetric Ca^{2+}-dependent vesicle export pathway from the peri-ER (not from normal ER membrane budding itself) to the plasma membrane; (2) the identification of MyoVa as a major Ca^{2+} sensor for ER Ca^{2+}, whose Ca^{2+}-dependent dissociation from ER Ca^{2+} channels triggers vesicle export; and (3) the physiological involvement of this membrane export pathway in chemotropic axon guidance in the developing nervous system. Specifically, we show that MyoVa directly senses spatially confined ER Ca^{2+} to control attractive axon guidance. Ca^{2+} triggers MyoVa dissociation from the RyR3 to facilitate asymmetric vesicle transport and exocytosis for growth cone attractive steering. Conversely, the impairment of this pathway causes repulsive turning responses to attractive signals. The prominent expression of ER channels and MyoVa in many cell types suggests the potential for broader involvement of this mechanism in cell morphogenesis and migration events beyond a role in neuronal axon guidance shown here.

Based on these findings, we propose a model where the co-localization of ER Ca^{2+} channels with MyoVa and their differential sensitivity to Ca^{2+} determine whether the attractive steering machinery is activated (Figure 8). Cytosolic Ca^{2+} concentrations ($[Ca^{2+}]_c$) in growth cones are approximately 50–200 nM under basal conditions (Henley and Poo, 2004; Ooashi et al., 2005) but increase up to several hundred nanomolar during repulsive turning induced by an extracellular cue or FLIP of caged Ca^{2+} (Henley et al., 2004; Ooashi et al., 2005). In this range of elevated $[Ca^{2+}]_c$, MyoVa is likely to remain associated with RyR3 because 2 μM or higher Ca^{2+} is necessary to dissociate MyoVa from RyR3

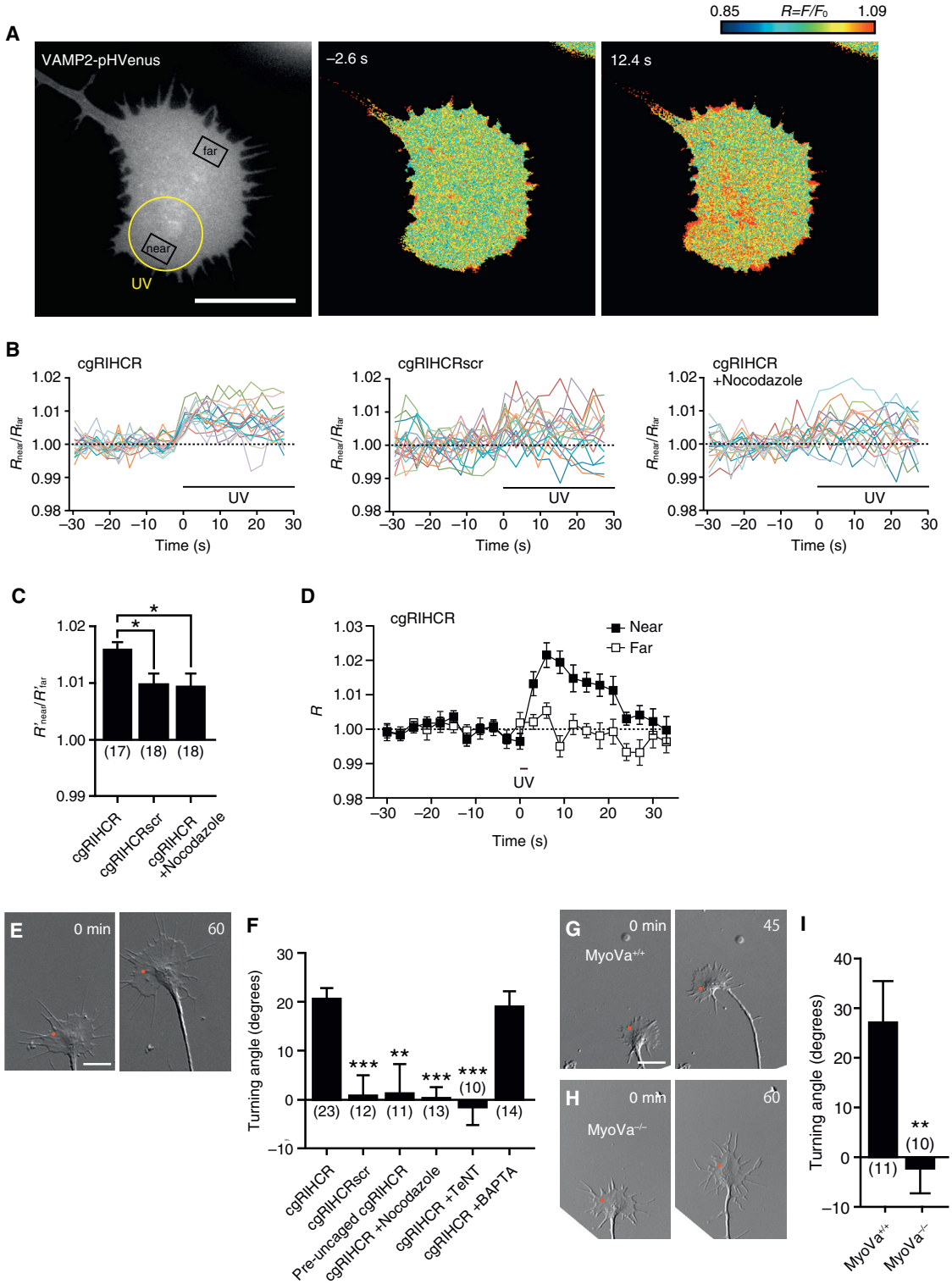

Figure 6. MyoVa Dissociation from ER Ca^{2+} Channels Drives VAMP2 Exocytosis and Growth Cone Turning

(A) Fluorescence images of a growth cone expressing VAMP2-pHVenus. The pseudo-color indicates relative fluorescence over the basal fluorescence (F/F_0; designated as R) before (−2.6 s) and after (12.4 s) the onset of repetitive photolysis of cgRIHCR (yellow circle in the leftmost image). Black boxes delineate the regions of interest (ROIs) used to quantify fluorescence intensities on the near and far sides of the growth cone. The scale bar represents 10 μm.

(B) Repetitive UV photolysis of cgRIHCR or cgRIHCRscr started at 0 min on the near side of growth cones in the absence or presence of nocodazole. R in each ROI was determined, and R on the near side divided by that on the far side was plotted against time. Each colored line represents R_{near}/R_{far} in a single growth cone.

(legend continued on next page)

(Figure 1). In contrast, such $[Ca^{2+}]_c$ elevations can be sufficient to trigger CICR, given that the open probability of purified RyR3 in planar lipid bilayers increases in the presence of 200 nM Ca^{2+} (Murayama et al., 1999). Whether Ca^{2+} opens RyR3 also depends on the activity of cyclic AMP (cAMP) (Ooashi et al., 2005): higher cAMP levels allow RyR3 to generate CICR in response to primary Ca^{2+} signals, whereas lower cAMP levels abolish CICR, thereby causing growth cones to show repulsive turning responses to Ca^{2+} signals. These findings are consistent with our model that physiological signals of several hundred nanomolar Ca^{2+} are insufficient for MyoVa activation but can trigger CICR if RyR3 is under the positive control of cAMP. Ca^{2+} concentrations inside the ER of DRG neurons are approximately 100–200 μM (Solovyova et al., 2002). When an ER Ca^{2+} channel opens, the peak $[Ca^{2+}]_c$ at a distance of 50 nm from the open channel reaches 5 μM as simulated mathematically (Rüdiger et al., 2007). Because our PLA data (Figure 4) suggest that MyoVa participates in the positioning of RyR3 and VAMP2 within 40 nm distance, it is reasonable to speculate that the intermolecular distance between MyoVa and RyR3 is sufficiently small for MyoVa to receive 5 μM or higher Ca^{2+} arising from CICR. This range of $[Ca^{2+}]$ can dissociate MyoVa from RyR3 possibly through MyoVa conformational changes driven by calmodulin release from MyoVa (Nguyen and Higuchi, 2005). In sum, our data suggest that MyoVa can respond specifically to ER-derived Ca^{2+}, thereby providing a molecular mechanism to discriminate between attractive and repulsive Ca^{2+} signals.

Whereas MyoVa dissociation from RyR3 can trigger centrifugal migration of VAMP2 vesicles, MyoVa itself could facilitate vesicle migration because the loss of MyoVa expression decreased the number of migrating vesicles in growth cones (Figure 3C). Consistent with this hypothesis, previous studies showed the presence of MyoVa-associated organelles on microtubules in growth cones (Evans et al., 1997) and suggested that electrostatic interactions between MyoVa and microtubules enhance the processivity of kinesin when both motors are present on the same cargo (Ali et al., 2008). Although we have not examined whether MyoVa remains associated with migrating vesicles after their departure from the ER, MyoVa could contribute to the kinesin-driven trafficking of vesicles along microtubules, in addition to its role as an ER Ca^{2+} sensor in this study.

Our peptide photolysis experiments (Figure 6) suggest that MyoVa dissociation from ER Ca^{2+} channels is sufficient to induce VAMP2-mediated exocytosis and growth cone attractive turning even in the absence of Ca^{2+} elevations. We suggest that centrifugal vesicle transport may be able to increase the pool size of exocytic vesicles in the growth cone P-domain, thereby potentiating the probability of spontaneous exocytosis. At presynaptic terminals, neurotransmitter release via vesicle exocytosis occurs in multiple modes including spontaneous release at resting $[Ca^{2+}]_c$ (Katz and Miledi, 1969) or even from neurons with intracellular Ca^{2+} chelated by BAPTA (Vyleta and Smith, 2011), and the probability of spontaneous release is positively correlated with the pool size of synaptic vesicles (Prange and Murphy, 1999). These mechanisms drawn from synaptic vesicle exocytosis are consistent with our model that the addition of VAMP2 vesicles to the pool on one side of the growth cone P-domain is sufficient to facilitate asymmetric exocytosis for attractive steering even in the absence of Ca^{2+} elevations.

In addition to its role in development, in the adult brain, ER-directed Ca^{2+}-driven export pathways may regulate synaptic plasticity. During the induction of long-term potentiation, AMPA receptor insertion requires MyoVa/Vb-dependent translocation of recycling endosomes that carry AMPA receptors into the spine (Correia et al., 2008; Wang et al., 2008). Although the involvement of ER-derived Ca^{2+} in this MyoVa/Vb-dependent process remains unclear, it is known that CICR elicits a fast and significant increase in the size of dendritic spines in cultured hippocampal neurons (Korkotian and Segal, 1999). Furthermore, MyoVa is reported to interact with the ER in Purkinje neurons and mobilizes ER into dendritic spines (Wagner et al., 2011). These findings point to an as yet untested functional role for ER-linked MyoVa in organelle transport for synaptic plasticity, with the dendritic ER as an important potential site for MyoVa action.

More broadly, many cell types other than neurons express both ER Ca^{2+} channels and MyoVa or related forms of myosin that could in principle regulate direct peri-ER to plasma membrane vesicle transport in motile and non-motile cells, in development or adult stages, and during disease progression such as tumor metastasis (Ouderkirk and Krendel, 2014). This export machinery may also operate during nerve regeneration and other forms of cell reprogramming and spatial sensing that would require directed membrane dynamics. Future studies should address both the broader verification of this pathway in other cell types and whether it can provide a useful target for regulation by therapeutic interventions to exert precise control over cell process morphology and migration in disease and damage.

(C) Quantification of data in (B). The y axis represents the ratio of R' on the near side to that on the far side (R'_{near}/R'_{far}), where R' is the mean of five consecutive R values after the onset of photolysis. Note that R'_{near}/R'_{far} is an index of asymmetric VAMP2 exocytosis across the growth cone after uncaging. Numbers in parentheses indicate the total number of growth cones examined. *$p < 0.05$.

(D) Time course changes in R on the near and far sides of 13 growth cones in response to single photolysis of cgRIHCR (100 ms in duration).

(E) Time-lapse DIC images of a growth cone, showing its turning response to cgRIHCR photolysis at red spots. Time in minutes after the onset of repetitive photolysis is shown. The scale bar represents 10 μm.

(F) Growth cones loaded with the indicated peptides were irradiated unilaterally with UV laser, and their turning responses were quantified. In some experiments, nocodazole or TeNT was bath applied or BAPTA loaded intracellularly. Positive and negative values represent growth cone turning toward and away from the side with laser irradiation, respectively. Numbers in parentheses indicate the total number of growth cones examined. **$p < 0.01$; ***$p < 0.001$ versus cgRIHCR.

(G and H) Time-lapse images of $MyoVa^{+/+}$ (G) and $MyoVa^{-/-}$ (H) growth cones, showing their responses to cgRIHCR photolysis at red spots. The scale bar represents 10 μm.

(I) Turning angles of $MyoVa^{+/+}$ and $MyoVa^{-/-}$ growth cones after cgRIHCR photolysis. **$p < 0.01$.

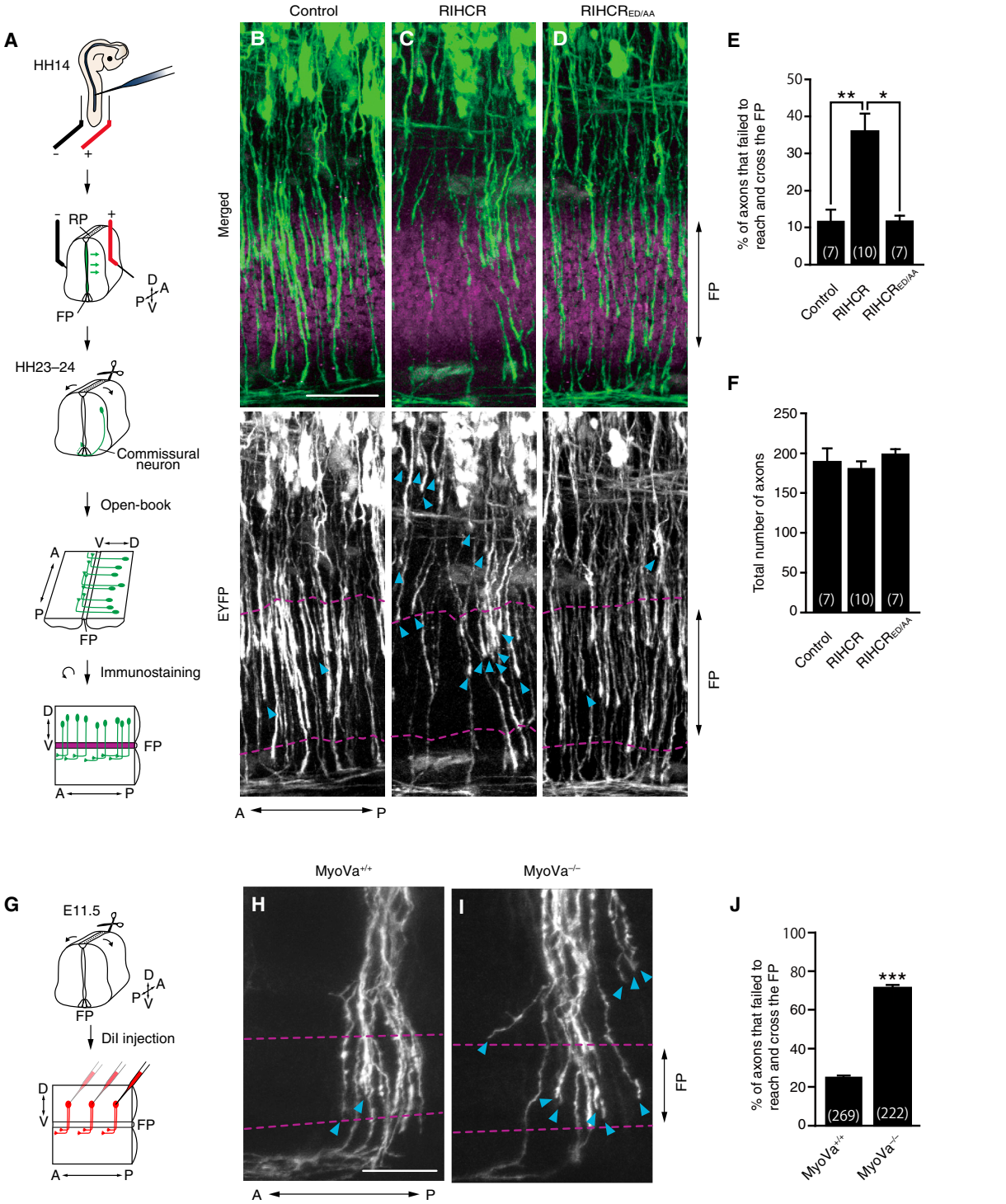

Figure 7. Commissural Axon Guidance Involves MyoVa Interaction with ER Ca^{2+} Channels

(A) Schematic diagram showing in ovo electroporation and an open-book preparation of the spinal cord to analyze commissural axon trajectories. Chick embryos were staged according to Hamburger and Hamilton (HH). A, anterior; D, dorsal; FP, floor plate; P, posterior; RP, roof plate; V, ventral.

(B–D) Projected z stack confocal images of open-book preparations showing commissural axons (EYFP; green) and the FP (HNF-3β immunofluorescence; magenta). Black and white images of EYFP are presented below corresponding merged images. The axons express EYFP alone (B; control), EYFP together with RIHCR (C), or EYFP with $RIHCR_{ED/AA}$ (D). Blue arrowheads point to the tips of axons that failed to reach and cross the FP. Magenta lines delineate the FP. The scale bar represents 50 μm.

(legend continued on next page)

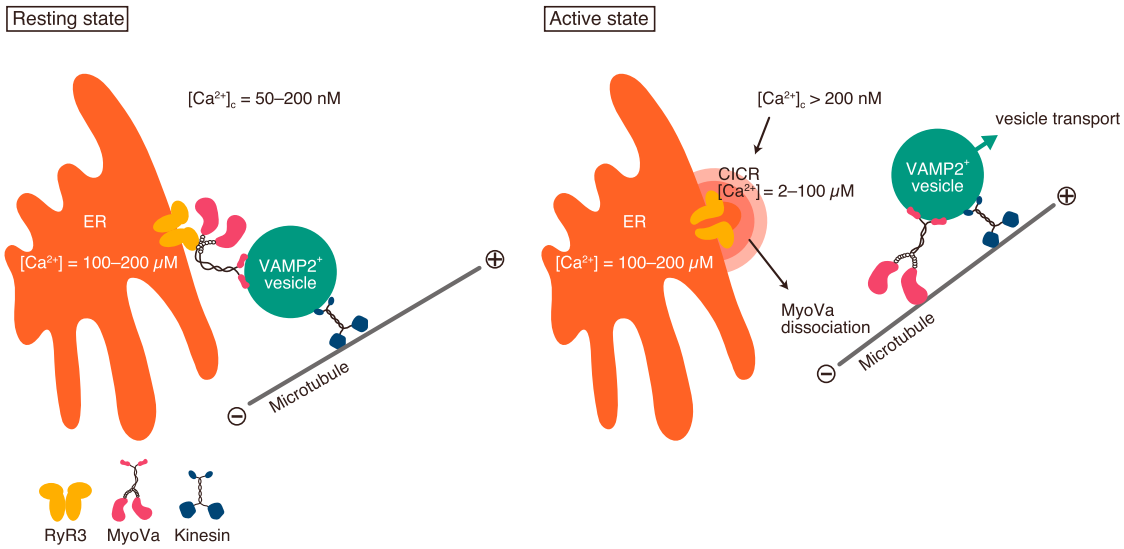

Figure 8. A Model of Ca^{2+} Microdomain Signaling on the ER

In the resting state (left panel), [Ca^{2+}] is maintained at 50–200 nM in the cytosol and 100–200 μM in the ER lumen. The neck of MyoVa remains associated with RyR3 in the absence of CICR. Primary Ca^{2+} elevations over 200 nM can activate RyR3, leading to the generation of CICR (right panel). CICR can increase [Ca^{2+}] over several micromolars in the close vicinity of open RyR3, which should be sufficient to dissociate MyoVa from this RyR3, thereby untethering a VAMP2-positive vesicle from the ER. Subsequently, dissociated MyoVa could facilitate kinesin-driven delivery of the vesicle toward the cell periphery and act as a Ca^{2+}-dependent sensor/effector of ER-derived Ca^{2+} for centrifugal membrane transport.

EXPERIMENTAL PROCEDURES

Mice

C57BL/6 mice were obtained from Japan SLC. RyR3$^{-/-}$ mice (provided by K. Mikoshiba; RIKEN BSI; Futatsugi et al., 1999) and DLS/LeJ mice (obtained from The Jackson Laboratory) were maintained at the RIKEN BSI Animal Care Facility. DLS/LeJ mice were genotyped by MyoVa immunoblotting. The experimental procedures and housing conditions for animals were approved by the Institute's Animal Experiments Committee of RIKEN and all of the animals were cared for and treated humanely in accordance with the Institutional Guidelines for Experiments Using Animals.

GST Pull-Down Assays and Mass Spectrometry

cDNA of mouse RyR3 RIHCR corresponding to amino acids 3,746–3,775 was inserted into the pGEX6P-1 (GE Healthcare). Site-directed RIHCR mutants were generated using a QuickChange II site-directed Mutagenesis kits (Agilent Technologies) with a set of primers (Table S1). GST-fused peptides were expressed and purified using Glutathione-Sepharose 4 Fast Flow (GE Healthcare). Brain lysates from postnatal day 0 (P_0) mice (C57BL/6) or HEK293T cell lysates were incubated with GST peptides, and bound proteins were subjected to SDS-PAGE followed by immunoblotting or mass spectrometry. Further details are provided in the Supplemental Experimental Procedures.

Antibodies

A detailed description of the antibodies used in this study is provided in the Supplemental Experimental Procedures.

cDNA Constructs and Transfection

Expression vectors for EGFP-fused MyoVa and its fragments were constructed using mouse cDNAs for full-length MyoVa (corresponding to amino acids 1–1,853), head (1–763), neck (764–910), P/M tail (911–1,443), or G-tail (1,444–1,853). EGFP cDNA followed by a sequence of these MyoVa fragments was inserted into a pCAG vector, a mammalian expression vector under the control of the CAG promoter (provided by J. Miyazaki, Osaka University; Niwa et al., 1991). Then, HEK293T cells were transfected transiently with these constructs using X-tremeGENE 9 DNA transfection reagent (Roche) according to the manufacturer's protocol. After 3 days, the cells were harvested and processed for GST pull-down assays.

For stable integration of electroporated transgenes in chick embryos, the Tol2 cassette (provided by Y. Takahashi; Nara Institute of Science and Technology; Sato et al., 2007) was inserted into a pCAG vector. We then inserted VAMP2-pHVenus cDNA between the Tol2 sequences, which encodes for a protein consisting of pHVenus fused to the luminal end of VAMP2. Similarly, we constructed an expression vector for VAMP2-iR-pHluorin, a protein consisting of iR-pHluorin (provided by A. Miyawaki, RIKEN BSI; Katayama et al., 2011) fused to the luminal end of VAMP2. For expression of mouse RIHCR

(E) Quantification of midline crossing of axons that express EYFP alone (control), RIHCR, or $RIHCR_{ED/AA}$. The y axis represents the percentage of axons that failed to reach and cross the FP. Numbers in parentheses indicate the total number of embryos examined. *$p < 0.05$; **$p < 0.01$.
(F) The total number of EYFP-positive axons in the specimens analyzed in (E).
(G) Schematic diagram showing DiI injections into an E11.5 mouse spinal cord open-book preparation to visualize commissural axon trajectories.
(H and I) Projected z stack confocal images of MyoVa$^{+/+}$ (H) and MyoVa$^{-/-}$ (I) open-book preparations. Commissural axons in each image were labeled by a single DiI spot. Blue arrowheads point to the tips of axons that failed to reach and cross the FP. The position of FP was determined on DIC images. The scale bar represents 50 μm.
(J) Quantification of midline crossing of DiI-labeled axons. The y axis represents the percentage of axons that failed to reach and cross the FP. Numbers in parentheses indicate the total number of DiI spots in six MyoVa$^{+/+}$ and six MyoVa$^{-/-}$ open-book preparations. We calculated the percentage per DiI spot and then SEM of 269 or 222 spots. ***$p < 0.001$.

and $RIHCR_{ED/AA}$, cDNAs for these peptides followed by sequences of internal ribosome entry site and EYFP were inserted into a pCAG vector under the control of the CAG promoter. Methods for in ovo electroporation are detailed in the Supplemental Experimental Procedures.

Cell Culture

DRGs from embryonic day 9 chickens or P_0 mice were dissociated and cultured as described previously (Ooashi et al., 2005). In some experiments, DRGs transfected in ovo were dissected, dissociated, and cultured.

HEK293T cells were cultured at 37°C with 5% CO_2 in DMEM (GIBCO) supplemented with 10% fetal bovine serum and penicillin-streptomycin mixed solution (Nacalai Tesque).

Intracellular Loading of Caged Compounds and Synthetic Peptides

A caged Ca^{2+} compound, *o*-nitrophenyl EGTA (NP-EGTA) (2 μM; Invitrogen), and a caged IP_3 compound, D-*myo*-inositol 1,4,5-triphosphate P^4,P^5-(1-(2-nitrophenyl)ethyl) ester (200 μM; Invitrogen), were loaded into DRG neurons as described previously (Akiyama et al., 2009; Ooashi et al., 2005). Chick RyR3 RIHCR peptide (5′-HDEFTRDLFRFLQLLCEGHNNDFQNYLRTQ-3′) and its derivatives, RIHCRscr (5′-HETDRFTNFLQRLCGLFQRLELFYHNNDQD-3′) and $RIHCR_{ED/AA}$ (5′-HDEFTRDLFRFLQLLCAGHNNAFQNYLRTQ-3′), were synthesized at the Support Unit for Bio-Material Analysis in RIKEN BSI Research Resources Center. Caged peptides were synthesized as detailed in the Supplemental Experimental Procedures. Synthetic peptides (260 μM) were introduced into DRG neurons by trituration loading (Akiyama et al., 2009). Alexa-Fluor-conjugated dextran (molecular weight 10,000; Invitrogen) was loaded simultaneously to allow for determination of neurons with positive loading. This method resulted in positive loading into 89.6% of 318 chick neurons and 49.4% of 320 mouse neurons.

Imaging of Membrane Trafficking

Imaging of FM1-43-labeled or VAMP2-iR-pHluorin-expressing vesicles in a growth cone was performed as described previously (Akiyama and Kamiguchi, 2010; Tojima et al., 2007). Caged compounds were photolyzed by exposing one side of the growth cone to UV light (<400 nm) from a xenon lamp passed through a pinhole as described previously (Tojima et al., 2007). We alternated the position of UV irradiation between the left and right sides when analyzing multiple growth cones. In some experiments, 10 nM nocodazole or 1 μM BAPTA-AM (Invitrogen) was applied to cultures at least 30 min before imaging. To enhance the outline of VAMP2-iR-pHluorin vesicles, fluorescence images were processed for unsharp masking using a custom-made MATLAB program (MathWorks) as follows: making two new images by applying Gaussian filters with different kurtosis to the background-subtracted image and subtracting the more-blurred image from the other.

To assess VAMP2-mediated exocytosis induced by xenon UV photolysis of caged peptides, asymmetric increases in VAMP2-pHVenus fluorescence across the growth cone was quantified as described previously (Tojima et al., 2007). Further details are provided in the Supplemental Experimental Procedures.

Immunoprecipitation and Immunoblotting

Brains from P_0 mice (C57BL/6) were extracted and incubated with anti-RyR3 or anti-IP_3R1 antibody immobilized to Dynabeads Protein G (VERITAS), and bound proteins were eluted with Laemmli sample buffer and subjected to immunoblotting. Further details are provided in the Supplemental Experimental Procedures. In some experiments, immunoprecipitation was performed in the presence of divalent cations ($CaCl_2$, $MgCl_2$, $BaCl_2$, or $SrCl_2$) or 100 μM peptides (chick RyR3 RIHCR peptide and its derivatives) added to brain extracts. Ca^{2+} concentrations in brain extracts were adjusted with an EGTA-Ca^{2+} buffer: 2 mM EGTA and appropriate concentrations of $CaCl_2$ determined using Maxchelator software (http://maxchelator.stanford.edu/CaEGTA-TS.htm).

PLA and Immunofluorescence

Formaldehyde-fixed and permeabilized cells as described previously (Tojima et al., 2007) were incubated with 10 μg/ml anti-RyR3 and 2 μg/ml anti-VAMP2 antibodies overnight at 4°C and then processed for either PLA or conventional immunofluorescence. PLA was performed using the Duolink PLA kit (Olink Bioscience) according to the manufacturer's protocol. For double immunofluorescence, the cells were incubated with Alexa-488- and 594-conjugated antibodies (10 μg/ml) to visualize VAMP2 and RyR3, respectively.

Axon Growth and Turning Assays

Growth cone turning induced by FLIP of caged compounds or by an extracellular gradient of MAG (R&D Systems) was performed as described previously (Akiyama et al., 2009; Ooashi et al., 2005; Tojima et al., 2010). The following reagents were applied to cultures at least 30 min before the experiments: 100 μM ryanodine (Alomone labs); 10 nM nocodazole (Merck); 5 nM TeNT (List); 1 or 5 μM EGTA-AM (Invitrogen); and 1 μM BAPTA-AM. Loading of EGTA-AM or BAPTA-AM was performed as described previously (Ooashi et al., 2005). To examine axon growth, neurons were cultured for 6 hr and the length of their axons measured as described previously (Kamiguchi and Yoshihara, 2001).

Analysis of Commissural Axon Trajectories in Open-Book Preparations

Open-book preparations of chick spinal cords were obtained as described previously (Stoeckli and Landmesser, 1995). Briefly, a chick embryo transfected in ovo at HH14 was sacrificed at HH23–24, and its spinal cord was opened at the roof plate followed by fixation with 4% paraformaldehyde in PBS and permeabilization with 0.1% Triton X-100 and 5% goat serum in PBS. The spinal cord was then incubated sequentially with anti-HNF-3β mouse monoclonal antibody (0.5 μg/ml) overnight at 4°C and Alexa-Fluor-594-conjugated secondary antibody (10 μg/ml) overnight at 4°C. Open-book preparations of E11.5 mouse spinal cords were fixed with 4% paraformaldehyde in PBS and subjected to iontophoretic injection of DiI (5 mg/ml; Molecular Probes) into the dorsal region as described previously (Birgbauer et al., 1995). The spinal cords were left for 48 hr to allow DiI anterograde labeling of commissural axons. Fluorescence images were acquired every 2 μm (chick) or 5 μm (mouse) along the z axis using a confocal microscope (FLUOVIEW FV1000 with IX81; Olympus), and a projection of approximately 30 optical sections was generated using FV10-ASW Version 4.1 (Olympus). Commissural axon trajectories were assessed by counting the number of axons that failed to reach and cross the FP.

Statistical Analyses

All data are expressed as the mean ± SEM. A single experimenter who was blind to the treatment conditions counted the number of membrane vesicles (Figures 3B, 3C, 3E, 5D, 5E, 5G, and S7), PLA puncta (Figure 4C), and commissural axons (Figures 7E, 7F, and 7J). Statistical analyses were performed using Prism Version 4.0b software (GraphPad). Statistical significance was assumed when $p < 0.05$. Further details are provided in the Supplemental Experimental Procedures.

SUPPLEMENTAL INFORMATION

Supplemental Information includes Supplemental Experimental Procedures, seven figures, one table, and three movies and can be found with this article online at http://dx.doi.org/10.1016/j.celrep.2016.04.021.

AUTHOR CONTRIBUTIONS

F.W. performed the experiments in Figures 1, 2, 3A–3C, 5A–5E, 6E–6I, S1, S2, S4, S6, and S7 and wrote the manuscript. A.N. performed the experiments in Figures 3D, 3E, 4, 5F, 5G, 6A–6D, 7, and S3. Y.T. synthesized caged peptides. N.O. performed the experiments in Figures 2D and S5. T.F. analyzed vesicle trajectories for Figure S6. T.N. conducted mass spectrometry. H.K. designed the research project, directed the experiments, and wrote the manuscript together with F.W.

ACKNOWLEDGMENTS

This work was supported by the Ministry of Education, Culture, Sports, Science and Technology of Japan (Grants-in-Aid for Challenging Exploratory

Research 23650196 to F.W. and for Scientific Research B 24300137 to H.K.). We are grateful to K. Mikoshiba for providing anti-IP_3R1 antibody and $RyR3^{-/-}$ mice; A. Miyawaki for iR-pHluorin construct; Y. Takahashi for Tol2 vectors; J. Miyazaki for pCAG vectors; A. Tamada for producing antisera against MyoVa; H. Akiyama, M. Inoue, I. Minoura, and H. Ito for technical assistance; and the RIKEN Brain Science Institute's Research Resources Center for experimental instruments. We also thank C. Yokoyama, A.V. Terashima, H. Akiyama, A.T. Guy, and J. Lai for valuable comments on this manuscript.

Received: March 26, 2015
Revised: March 11, 2016
Accepted: March 31, 2016
Published: April 28, 2016

REFERENCES

Akiyama, H., and Kamiguchi, H. (2010). Phosphatidylinositol 3-kinase facilitates microtubule-dependent membrane transport for neuronal growth cone guidance. J. Biol. Chem. *285*, 41740–41748.

Akiyama, H., Matsu-ura, T., Mikoshiba, K., and Kamiguchi, H. (2009). Control of neuronal growth cone navigation by asymmetric inositol 1,4,5-trisphosphate signals. Sci. Signal. *2*, ra34.

Ali, M.Y., Lu, H., Bookwalter, C.S., Warshaw, D.M., and Trybus, K.M. (2008). Myosin V and Kinesin act as tethers to enhance each others' processivity. Proc. Natl. Acad. Sci. USA *105*, 4691–4696.

Birgbauer, E., Sechrist, J., Bronner-Fraser, M., and Fraser, S. (1995). Rhombomeric origin and rostrocaudal reassortment of neural crest cells revealed by intravital microscopy. Development *121*, 935–945.

Correia, S.S., Bassani, S., Brown, T.C., Lisé, M.F., Backos, D.S., El-Husseini, A., Passafaro, M., and Esteban, J.A. (2008). Motor protein-dependent transport of AMPA receptors into spines during long-term potentiation. Nat. Neurosci. *11*, 457–466.

Dickson, B.J., and Zou, Y. (2010). Navigating intermediate targets: the nervous system midline. Cold Spring Harb. Perspect. Biol. *2*, a002055.

Eggermann, E., Bucurenciu, I., Goswami, S.P., and Jonas, P. (2011). Nanodomain coupling between Ca^{2+} channels and sensors of exocytosis at fast mammalian synapses. Nat. Rev. Neurosci. *13*, 7–21.

Espreafico, E.M., Cheney, R.E., Matteoli, M., Nascimento, A.A., De Camilli, P.V., Larson, R.E., and Mooseker, M.S. (1992). Primary structure and cellular localization of chicken brain myosin-V (p190), an unconventional myosin with calmodulin light chains. J. Cell Biol. *119*, 1541–1557.

Evans, L.L., Hammer, J., and Bridgman, P.C. (1997). Subcellular localization of myosin V in nerve growth cones and outgrowth from dilute-lethal neurons. J. Cell Sci. *110*, 439–449.

Fukuda, M., Kuroda, T.S., and Mikoshiba, K. (2002). Slac2-a/melanophilin, the missing link between Rab27 and myosin Va: implications of a tripartite protein complex for melanosome transport. J. Biol. Chem. *277*, 12432–12436.

Futatsugi, A., Kato, K., Ogura, H., Li, S.T., Nagata, E., Kuwajima, G., Tanaka, K., Itohara, S., and Mikoshiba, K. (1999). Facilitation of NMDAR-independent LTP and spatial learning in mutant mice lacking ryanodine receptor type 3. Neuron *24*, 701–713.

Gomez, T.M., and Zheng, J.Q. (2006). The molecular basis for calcium-dependent axon pathfinding. Nat. Rev. Neurosci. *7*, 115–125.

Hamburger, V., and Hamilton, H.L. (1951). A series of normal stages in the development of the chick embryo. J. Morphol. *88*, 49–92.

Hammer, J.A., 3rd, and Sellers, J.R. (2011). Walking to work: roles for class V myosins as cargo transporters. Nat. Rev. Mol. Cell Biol. *13*, 13–26.

Henley, J., and Poo, M.M. (2004). Guiding neuronal growth cones using Ca^{2+} signals. Trends Cell Biol. *14*, 320–330.

Henley, J.R., Huang, K.H., Wang, D., and Poo, M.M. (2004). Calcium mediates bidirectional growth cone turning induced by myelin-associated glycoprotein. Neuron *44*, 909–916.

Hong, K., Nishiyama, M., Henley, J., Tessier-Lavigne, M., and Poo, M. (2000). Calcium signalling in the guidance of nerve growth by netrin-1. Nature *403*, 93–98.

Huber, A.B., Kolodkin, A.L., Ginty, D.D., and Cloutier, J.F. (2003). Signaling at the growth cone: ligand-receptor complexes and the control of axon growth and guidance. Annu. Rev. Neurosci. *26*, 509–563.

Kamiguchi, H., and Yoshihara, F. (2001). The role of endocytic l1 trafficking in polarized adhesion and migration of nerve growth cones. J. Neurosci. *21*, 9194–9203.

Katayama, H., Kogure, T., Mizushima, N., Yoshimori, T., and Miyawaki, A. (2011). A sensitive and quantitative technique for detecting autophagic events based on lysosomal delivery. Chem. Biol. *18*, 1042–1052.

Katz, B., and Miledi, R. (1969). Spontaneous and evoked activity of motor nerve endings in calcium Ringer. J. Physiol. *203*, 689–706.

Korkotian, E., and Segal, M. (1999). Release of calcium from stores alters the morphology of dendritic spines in cultured hippocampal neurons. Proc. Natl. Acad. Sci. USA *96*, 12068–12072.

Lokuta, A.J., Komai, H., McDowell, T.S., and Valdivia, H.H. (2002). Functional properties of ryanodine receptors from rat dorsal root ganglia. FEBS Lett. *511*, 90–96.

Mercer, J.A., Seperack, P.K., Strobel, M.C., Copeland, N.G., and Jenkins, N.A. (1991). Novel myosin heavy chain encoded by murine dilute coat colour locus. Nature *349*, 709–713.

Murayama, T., Oba, T., Katayama, E., Oyamada, H., Oguchi, K., Kobayashi, M., Otsuka, K., and Ogawa, Y. (1999). Further characterization of the type 3 ryanodine receptor (RyR3) purified from rabbit diaphragm. J. Biol. Chem. *274*, 17297–17308.

Nguyen, H., and Higuchi, H. (2005). Motility of myosin V regulated by the dissociation of single calmodulin. Nat. Struct. Mol. Biol. *12*, 127–132.

Niwa, H., Yamamura, K., and Miyazaki, J. (1991). Efficient selection for high-expression transfectants with a novel eukaryotic vector. Gene *108*, 193–199.

Ohyama, A., Komiya, Y., and Igarashi, M. (2001). Globular tail of myosin-V is bound to vamp/synaptobrevin. Biochem. Biophys. Res. Commun. *280*, 988–991.

Ooashi, N., Futatsugi, A., Yoshihara, F., Mikoshiba, K., and Kamiguchi, H. (2005). Cell adhesion molecules regulate Ca^{2+}-mediated steering of growth cones via cyclic AMP and ryanodine receptor type 3. J. Cell Biol. *170*, 1159–1167.

Ouderkirk, J.L., and Krendel, M. (2014). Non-muscle myosins in tumor progression, cancer cell invasion, and metastasis. Cytoskeleton (Hoboken) *71*, 447–463.

Parekh, A.B. (2008). Ca^{2+} microdomains near plasma membrane Ca^{2+} channels: impact on cell function. J. Physiol. *586*, 3043–3054.

Parra, L.M., and Zou, Y. (2010). Sonic hedgehog induces response of commissural axons to Semaphorin repulsion during midline crossing. Nat. Neurosci. *13*, 29–35.

Ponting, C.P. (2000). Novel repeats in ryanodine and IP_3 receptors and protein *O*-mannosyltransferases. Trends Biochem. Sci. *25*, 48–50.

Prange, O., and Murphy, T.H. (1999). Correlation of miniature synaptic activity and evoked release probability in cultures of cortical neurons. J. Neurosci. *19*, 6427–6438.

Reck-Peterson, S.L., Provance, D.W., Jr., Mooseker, M.S., and Mercer, J.A. (2000). Class V myosins. Biochim. Biophys. Acta *1496*, 36–51.

Rüdiger, S., Shuai, J.W., Huisinga, W., Nagaiah, C., Warnecke, G., Parker, I., and Falcke, M. (2007). Hybrid stochastic and deterministic simulations of calcium blips. Biophys. J. *93*, 1847–1857.

Sato, Y., Kasai, T., Nakagawa, S., Tanabe, K., Watanabe, T., Kawakami, K., and Takahashi, Y. (2007). Stable integration and conditional expression of electroporated transgenes in chicken embryos. Dev. Biol. *305*, 616–624.

Söderberg, O., Gullberg, M., Jarvius, M., Ridderstråle, K., Leuchowius, K.J., Jarvius, J., Wester, K., Hydbring, P., Bahram, F., Larsson, L.G., and

Landegren, U. (2006). Direct observation of individual endogenous protein complexes *in situ* by proximity ligation. Nat. Methods *3*, 995–1000.

Solovyova, N., Veselovsky, N., Toescu, E.C., and Verkhratsky, A. (2002). $Ca^{(2+)}$ dynamics in the lumen of the endoplasmic reticulum in sensory neurons: direct visualization of $Ca^{(2+)}$-induced $Ca^{(2+)}$ release triggered by physiological $Ca^{(2+)}$ entry. EMBO J. *21*, 622–630.

Stoeckli, E.T., and Landmesser, L.T. (1995). Axonin-1, Nr-CAM, and Ng-CAM play different roles in the in vivo guidance of chick commissural neurons. Neuron *14*, 1165–1179.

Tessier-Lavigne, M., and Goodman, C.S. (1996). The molecular biology of axon guidance. Science *274*, 1123–1133.

Tojima, T., Akiyama, H., Itofusa, R., Li, Y., Katayama, H., Miyawaki, A., and Kamiguchi, H. (2007). Attractive axon guidance involves asymmetric membrane transport and exocytosis in the growth cone. Nat. Neurosci. *10*, 58–66.

Tojima, T., Itofusa, R., and Kamiguchi, H. (2010). Asymmetric clathrin-mediated endocytosis drives repulsive growth cone guidance. Neuron *66*, 370–377.

Tojima, T., Hines, J.H., Henley, J.R., and Kamiguchi, H. (2011). Second messengers and membrane trafficking direct and organize growth cone steering. Nat. Rev. Neurosci. *12*, 191–203.

Tojima, T., Itofusa, R., and Kamiguchi, H. (2014). Steering neuronal growth cones by shifting the imbalance between exocytosis and endocytosis. J. Neurosci. *34*, 7165–7178.

Vyleta, N.P., and Smith, S.M. (2011). Spontaneous glutamate release is independent of calcium influx and tonically activated by the calcium-sensing receptor. J. Neurosci. *31*, 4593–4606.

Wagner, W., Brenowitz, S.D., and Hammer, J.A., 3rd. (2011). Myosin-Va transports the endoplasmic reticulum into the dendritic spines of Purkinje neurons. Nat. Cell Biol. *13*, 40–48.

Wang, Z., Edwards, J.G., Riley, N., Provance, D.W., Jr., Karcher, R., Li, X.D., Davison, I.G., Ikebe, M., Mercer, J.A., Kauer, J.A., and Ehlers, M.D. (2008). Myosin Vb mobilizes recycling endosomes and AMPA receptors for postsynaptic plasticity. Cell *135*, 535–548.